Modeling the Posteruptive Deformation at Okmok Based on the GPS and InSAR Time Series: Changes in the Shallow Magma Storage System

Xueming Xue[1] , Jeff Freymueller[1] , and Zhong Lu[2]

[1]Department of Earth and Environmental Sciences, Michigan State University, East Lansing, MI, USA, [2]Roy M. Huffington Department of Earth Sciences, Southern Methodist University, Dallas, TX, USA

Abstract Based on the unscented Kalman filter, we develop a time-dependent inversion filter combining Global Positioning System (GPS) and Interferometric Synthetic Aperture Radar (InSAR) time series observations for modeling volcano deformation. We use the Variance Component Estimation method as means to assign the relative weights for GPS and InSAR data. Then we use the inversion filter to model the posteruptive deformation at Okmok volcano, Alaska. We find that a Mogi source at 3–4 km depth fits the InSAR data well, while the best fit to the GPS data is an oblate spheroid source at about 2.5 km depth. Our final model consists of a shallow sill at ~0.9 km and a Mogi source at ~3.2 km depth, which well fit both the GPS and InSAR data simultaneously. We think the Mogi source obtained here is the same source account for the preeruptive deformation. The shallow sill is a new structure that was not seen before the 2008 eruption. From 2008 to 2019, we have observed five inflation episodes, each of which decays exponential in time. We find that the characteristic timescale of those inflation episodes decreases with respect to time. The total volume change from the two sources is 0.068 km^3, which recovers 50–60% of the volume decrease during the 2008 eruption.

1. Introduction

1.1. Okmok Volcano and Its Recent Eruptions

Okmok volcano is one of the most active volcanoes in the central Aleutian arc, Alaska. Within the past century, significant eruptions occurred in 1945, 1958, and 1997 (Miller et al., 1998). These events were all effusive eruptions originating from Cone A (Figure 1). The most recent eruption occurred in 2008 from 12 July to late August. There are many differences between the 2008 eruption and the previous three events. First, the 2008 eruption opened a new cone, Ahmanilix, close to Cone D but far from Cone A. Second, it was more phreatomagmatic rather than effusive, indicating the 2008 eruption was involved with water to a great extent. Several hundred million cubic meters of ash and tephra deposits were ejected during the eruption and blanketed the whole caldera and part of the northeastern flank. Third, the size of the 2008 eruption was bigger than the previous historical eruptions. It produced a minimum dense rock equivalent volume of 0.17 km^3 that is about 3 times larger than the volumes of the 1958 and 1997 eruptions (Larsen et al., 2015). The geodetic models also show that the total magma volume decrease during the 2008 eruption was 2–3 times larger than the volume decrease during the 1997 eruption (Lu & Dzurisin, 2010).

Persistent ground deformation has also been observed between the eruptions at Okmok volcano. Fournier et al. (2009) inverted 6 years of continuous and campaign Global Positioning System (GPS) data and found a stable Mogi source at ~2.6 km depth. Lu et al. (2010) analyzed 150 Interferometric Synthetic Aperture Radar (InSAR) images between the 1997 and the 2008 eruptions and found a Mogi source at ~3 km depth. Biggs et al. (2010) analyzed a combined data set including more than 15 years of InSAR and continuous GPS measurement and found that all pre-2008 data could be explained well by a single Mogi source at 3.4 km depth. These studies, no matter what data are used, indicate that all the deformation before the 2008 eruption can be explained by a single Mogi source centered beneath the caldera at ~3 km depth. As for the posteruptive source model, Freymueller and Kaufman (2010) found that a shallower source than the preeruptive source located at 1.9 km depth was best to interpret the coeruptive and early posteruptive deformation based on GPS measurements. However, Qu et al. (2015) inverted the posteruptive InSAR time series observations from 2008 to 2014 and found a source at ~3.9 km depth, apparently twice as deep as the
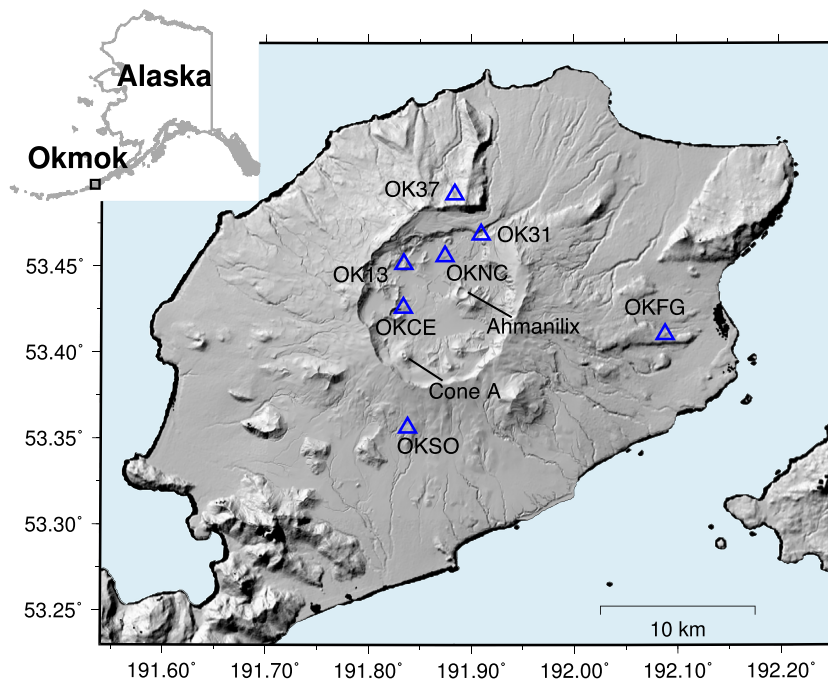
Figure 1. Location and shaded relief map of Okmok volcano. Cone A, Cone Ahmanilix, and the GPS sites used in our study are labeled.

GPS estimated source. Although these two studies focused on different time windows, the source locations they determined seem to be too different, which prompts a further study to determine the source geometry for the posteruptive period.

1.2. Time-Dependent Inversion Filters

It is always better to take advantage of time series observations, which capture the temporal evolution of the source model and then can help us understand the magma dynamics. The most common way to utilize time series observations is through a time-dependent inversion filter. Compared to least squares methods, inversion filters invert the time series of observations in a sequential way and demand much less computational cost. There have been a lot of efforts made to develop such techniques. The pioneering application in geodesy is the network inversion filter (NIF), which is essentially a linear Kalman filter. The NIF was first proposed to study slow slip sequences and has been successfully applied in many cases (e.g., Bartlow et al., 2014; Bekaert et al., 2016; Segall & Matthews, 1997). The extended NIF is then developed to simultaneously estimate the slip distribution and Laplacian smoothing factor based on the extended Kalman filter that linearizes the system by calculating the Jacobians (McGuire & Segall, 2003). Although the extended NIF can deal with nonlinear systems, there will be usually unpredictable errors when linearizing highly nonlinear systems that are exactly the case for most volcanic source models. Apparently, the NIFs are not suitable to invert for volcanic sources because the forward models of volcano deformation are usually highly nonlinear. Another extension of the Kalman filter, called the unscented Kalman filter (UKF), was later introduced to model volcano deformation by Fournier et al. (2009). They developed an inversion filter that was able to model GPS time series and then recovered the kinemics of the volcanic source at Okmok volcano from 2004 to 2008. Instead of calculating the exact Jacobians, the UKF approximates the Jacobians of the nonlinear model by passing through a set of sigma point selected based on a method called the unscented transformation (Julier & Uhlmann, 2004; Wan & Van Der Merwe, 2000). In this study, we will extend the work of Fournier et al. (2009) by making the UKF be able to combine GPS and InSAR measurements. Readers should refer to Fournier et al. (2009) or Julier and Uhlmann (2004) for technical details about UKF.

Gregg and Pettijohn (2016) recently introduced a data assimilation framework for inverting volcanic sources using finite element models and the ensemble Kalman filter (EnKF). Their method has been also

demonstrated to be effective studying real data sets (Albright et al., 2019; Zhan et al., 2017). The EnKF does not calculate the Jacobians explicitly either. It approximates the Jacobians of the nonlinear system using an ensemble of models, which are sampled by the use of the Monte Carlo Markov Chain method. Both the UKF and EnKF will perform well when the models are highly nonlinear, but we chose to use UKF in this work because Fournier et al. (2009) have demonstrated that it is effective for this kind of problem. In addition, the UKF is more efficient when using simple models although both the UKF and EnKF can be expected to perform well and give equivalent results. The number of sampling points used in the UKF is $2n + 1$, where n is the number of unknown parameters, and thus, for our problem with very few parameters the number of samples required is small. When n becomes very large, the UKF becomes less efficient than the EnKF because the number of models needed in the EnKF ensemble is less dependent on the number of unknown parameters. Gregg and Pettijohn (2016) recommended using between 50 and 200 models in the ensemble with the EnKF. Also, it requires a significant convergence time, although this should decrease as the number of models in the ensemble decreases. We expect that the EnKF should perform better after reaching convergence for finite element models with a larger number of parameters.

2. Data

2.1. GPS Data

GPS measurements record the displacement of an in situ monument in three dimensions (east, north, and up). The posteruptive GPS network at Okmok volcano is composed of seven sites (Figure 1). Among them, OKCE, OKSO, and OKFG are continuous sites installed in 2002 and OKNC was built in 2010 after the eruption (Figure 2a). The OK13, OK31, and OK37 are temporary sites surveyed for several months right after the eruption and were resurveyed in the summer of 2010. Data availability in time is shown in Figure 2c. All the GPS data were processed based on daily solutions and transformed into ITRF2008, using the approach of Fu and Freymueller (2012). Following Fournier et al. (2009), we use weekly averaged positions and rescale the noise covariance based on the short-term scatter. The scaling factor is 4.5.

We use the baselines relative to OKFG instead of the absolute displacements. First, the GPS network is not robust enough for the inversion filter to directly estimate regional velocity. OKFG is the only site located far from the caldera center, and most of the signals recorded should be nonvolcanic deformation. By using the baseline observations, we avoid estimating the regional velocity and can have a better constraint on the volcanic sources. Additionally, deeper deflation was observed at OKFG during the first year after the eruption (Freymueller & Kaufman, 2010). These deflation signals may reflect activities of deeper magma sources. It is not likely that we can have a reliable estimation for that with our data. Using the baseline measurements also remove the signals from potential much deep sources so that we can have stronger constraints on the shallow sources that we will focus on in this paper.

Note that the GPS measurement equation (which will be later discussed in section 3.2) when using baseline measurements should be written as $\mathbf{d}_{\text{baseline}} = g(\mathbf{m}) - g_{\text{OKFG}}(\mathbf{m})$, where g is the forward model of a volcanic source model. The GPS measurements mentioned in the rest of this paper refers to the baseline measurement relative to OKFG.

2.2. InSAR Data

InSAR measurements record the displacement of a coherent pixel on the ground in the line-of-sight direction to a remote sensing satellite. We use the InSAR data from Envisat ascending track 222 (E222), Envisat descending track 115 (E115), TerraSAR ascending track 116 (T116), and TerraSAR descending track 93 (T93) (Figure 2b). The Envisat data are available until 2010, and the TerraSAR data are available until 2014 (Figure 2c). The data were processed by Qu et al. (2015), and readers are referred to that paper for details on satellite information and data processing. We use their data but mask out the InSAR coherent pixels inside the caldera (Figure 2b) because we find that the InSAR data would be fit more poorly if those pixels are included, and there are systematic postfit residuals inside the caldera. We infer that these residuals represent actual surficial deformation related to the thick tephra deposits from the 2008 eruption (see section 6.1).

Unlike GPS, the uncertainties of InSAR data are not directly given and it is not trivial to include InSAR uncertainties in the time-dependent inversion filter. The InSAR uncertainties describe the observation noise, which are mainly caused by atmospheric delays and are spatially correlated. They are assumed to follow a
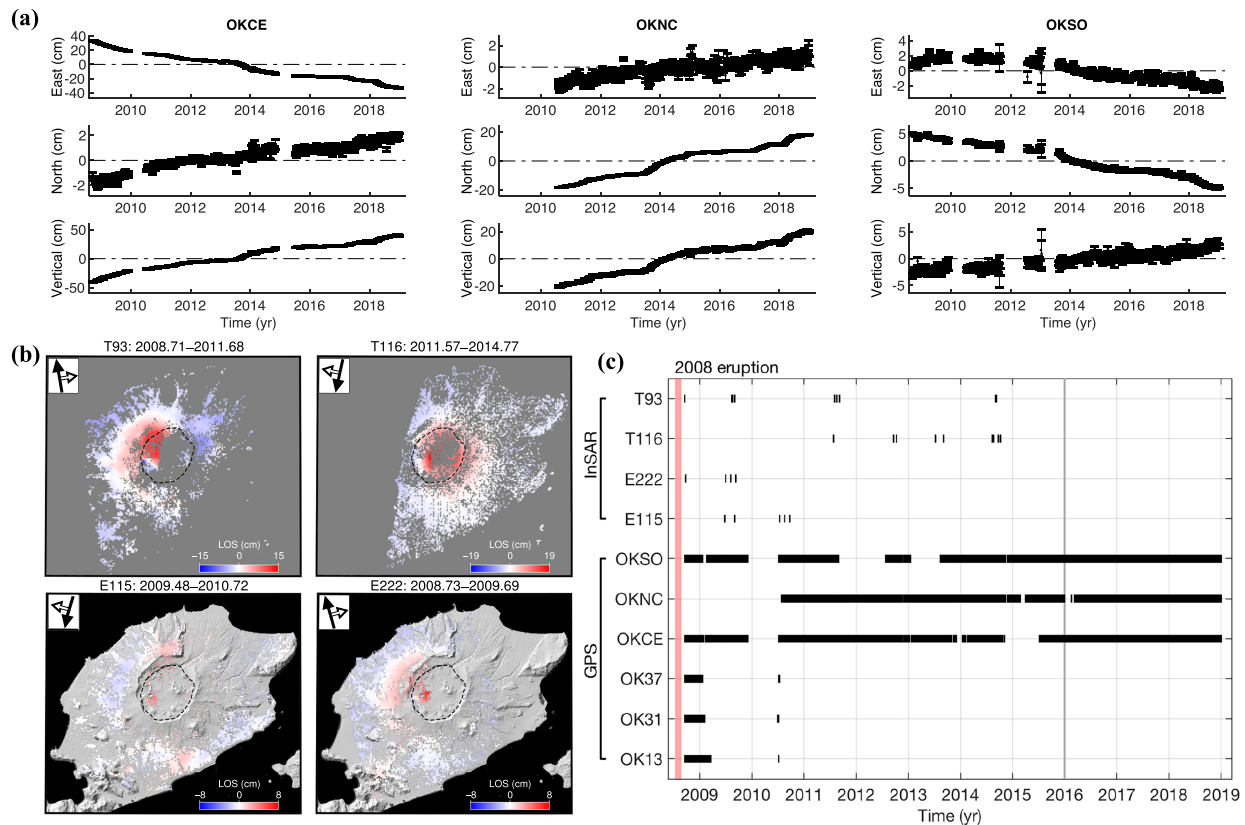
Figure 2. (a) Baseline measurements from the three continuous sites OKCE, OKNC, and OKSO relative to the site OKFG. (b) Examples of the InSAR data from each track showing line-of-sight displacements. Black arrow on the top left panel is satellite azimuth, and white arrow is satellite look angle. (c) Data availability in time. Each bar represents a data point. The gray line separates the GPS data into two parts. The data from 2008 to 2016 are used in the combination with InSAR mainly to determine the source geometry, and the data after are used only for the volume change estimation (see section 5).

Gaussian distribution, with correlations between nearby pixels so that the covariance matrix is fully populated instead of diagonal. Here we use the method of sample semivariogram and semicovariogram to construct the variance-covariance matrix for each interferogram (Lohman & Simons, 2005). First, we estimate a Mogi source and a linear phase ramp for each original interferogram using least squares. The residuals should be mainly the errors. We then carry out the error analysis on the residuals. The parameters for constructing the variance-covariance matrix of each interferogram are listed in Table S1 in the supporting information. Finally, we resample all the interferograms using the quadtree method (Simons et al., 2002) and propagate the corresponding variance-covariance matrix. These downsampled interferograms, with their variance-covariance matrix, are used in any time-dependent inversions of this study.

3. Time-Dependent Inversion Method

3.1. Volcanic Source Models

In this study, we use the analytical model that calculates the deformation from an arbitrary oriented spheroid (Cervelli, 2013) but we simplify the model to make the inversions more robust. First, we fix the dip to 90° to only estimate a vertical oriented spheroid source. In this case, the strike becomes a dummy variable. Then, we estimate the ratio of the vertical to the horizontal axis instead of the absolute semi-axes dimensions (a point source assumption), which allows us to know the shape but not the actual size of the source. The point source assumption is valid when the size of the source is small enough compared to its depth. For very shallow sources, the point source assumption would be incorrect. We have tested if the point source assumption is valid when the source is estimated to be shallow enough.

The simplified model then determines a vertically oriented spheroid using five parameters: location (east, north, and vertical), volume change, and axis ratio. This model is equivalent to a Mogi source when the axis ratio equals to 1 (Mogi, 1958). When the ratio is larger than 1, the model is a prolate spheroidal source (Yang et al., 1988). When the ratio is smaller than 1, the model is equivalent to an oblate spheroidal source when the ratio is less than 1. When the ratio is much less than 1 (e.g., 0.01), the model approximates a penny-shaped crack source or so called circular sill (Fialko et al., 2001). We present the source strength in terms of volume change. This is an interpretation that the pressure changes are due to increasing the volume of the reservoir by adding new magma.

3.2. Nuisance Parameters Associated With the Measurements

While always the same source parameters, different nuisance parameters will be estimated for different types of data. For GPS data, an initial position for each component (east, north and vertical) is estimated along with the volcanic source parameters. As we are using baseline observations, we do not need to estimate a regional velocity or frame translation but we estimate a common mode error for all GPS data. The source of common mode could be the partitioning between OKFG and other sites due to the slab subduction, considering that OKFG is more than 10 km apart and is closer to the Aleutian trench.

For InSAR data, two types of nuisance parameters are estimated. One is the linear phase ramp. As the phase ramps should not be correlated in time, they are estimated as white noise. The other type of nuisance parameter is the initial volume change, which represents the volume change at the reference acquisition time of each track. They are estimated as a constant. If more than one source is modeled in the UKF, an initial volume change will be estimated for each source. For the sake of reducing the number of unknown parameters, the initial volume change parameters can be shared by multiple InSAR time series if their starting times are the same or very close (e.g., shorter than 1 week). This is not vital but can help reduce the total number of unknown parameters, especially when modeling multiple sources. In this study, we only estimate one set of initial volume change parameter for both T93 and E222 as their reference acquisition times are in the same week.

Given one GPS time series and one InSAR time series, now we can write the state transition equation with the process noise as below

$$
\begin{bmatrix} \mathbf{m}_k \\ \mathbf{c}_k \\ \mathbf{d}_0 \\ \mathbf{r}_k \\ V_0 \end{bmatrix} = \begin{bmatrix} \mathbf{I} & & & & \\ & \mathbf{0} & & & \\ & & \mathbf{I} & & \\ & & & 0 & \\ & & & & 1 \end{bmatrix} \begin{bmatrix} \mathbf{m}_{k-1} \\ \mathbf{c}_{k-1} \\ \mathbf{d}_0 \\ \mathbf{r}_{k-1} \\ V_0 \end{bmatrix}, \mathbf{Q_k} = \begin{bmatrix} \Delta t_k \delta_{\mathbf{m}}^2 & & & & \\ & \delta_{\mathbf{c}}^2 & & & \\ & & \mathbf{0} & & \\ & & & \delta_{\mathbf{r}}^2 & \\ & & & & 0 \end{bmatrix} \tag{1}
$$

where $\mathbf{m}$ is general source model parameters; $\mathbf{c}$ is the common mode for all GPS time series; $\mathbf{d}_0$ is the initial position for each site; $\mathbf{r}$ is the linear phase ramp; V_0 is the reference volume change for the InSAR time series; and $\mathbf{I}$ is the identity matrix. The process noise deviation is denoted as δ. The corresponding measurement equation at a certain epoch can be written as below

$$
\begin{bmatrix} \mathbf{d}_{\mathrm{GPS}} \\ \mathbf{d}_{\mathrm{InSAR}} \end{bmatrix} = \begin{bmatrix} G(\mathbf{m}, \mathbf{x}_{\mathrm{GPS}}) + \mathbf{c} + \mathbf{d}_0 \\ G(\mathbf{m}, V_0, \mathbf{x}_{\mathrm{InSAR}}) + \mathbf{Lr} \end{bmatrix}, \mathbf{R} = \begin{bmatrix} \sigma^{\mathbf{GPS}} \epsilon_{\mathrm{GPS}}^2 & \\ & \sigma^{\mathbf{InSAR}} \epsilon_{\mathrm{InSAR}}^2 \end{bmatrix} \tag{2}
$$

where $\mathbf{d}$ is the data; ϵ is the data noise deviation; $\mathbf{x}$ is the measurement location; $\mathbf{Lr}$ represents a linear phase ramp where $\mathbf{L} = \begin{bmatrix} \mathbf{I} & \mathbf{x}_1^{\mathbf{InSAR}} & \mathbf{x}_2^{\mathbf{InSAR}} \end{bmatrix}$; and G is the forward model. The scaling factor of the noise covariance matrix is $\sigma^{\mathbf{GPS}}$ for GPS data and $\sigma^{\mathbf{InSAR}}$ for InSAR data. Other symbols are same as in equation (1).

As the time interval of InSAR time series can be large, Bekaert et al. (2016) introduced pseudo observations when integrating InSAR data into the NIF. In practice, it is also helpful to use pseudo observations for InSAR data in the UKF. The pseudo observations essentially provide additional constraints on the initial/reference volume change and then help calibrate all the InSAR data to the same time frame along with GPS data. Bekaert et al. (2016) generated the pseudo observations to be all zeros. We find that this may be robust for the linear inversion filters (i.e., the network inversion filter) but may cause numerical instabilities for a

nonlinear inversion filter (i.e., the UKF). Here we generate InSAR pseudo observations from a normal distribution with zero mean and very small deviation (e.g., 1e−6).

3.3. Initialization and Hyperparameter Tuning

An inappropriate prior or initialization could cause the divergence of the UKF. However, based on extensive testing for this problem, it is not necessary to give a highly accurate prior because a reasonable prior is easy to obtain, and a prior with uncertainty of a few kilometers for the horizontal location and 1–2 km for the source depth ensured rapid convergence. In choosing the sigma points for the UKF, we used hyperparameters determined by Fournier et al. (2009), which also worked well for the similar source models used in this study, and convergence of the UKF was not sensitive to variations in these hyperparameters.

It is much more important to determine the optimal hyperparameters (i.e., δ_m, δ_c and δ_r) that control the temporal smoothness of the corresponding unknown parameters. A larger hyperparameter allows the parameter to change faster in time but could cause overfitting of noise in the data. A smaller hyperparameter makes the parameter change slower but could cause underfitting of the data. We find that the values of δ_c and δ_r for the nuisance parameters do not impact much the final results, so we simply set $\delta_c = [10,10,10]$ (mm) and $\delta_c = [100,1,1]$ (mm, mm/km, mm/km). The values of δ_m for the source parameter plays a much more significant role on the final estimates. There are two typical methods used to obtain the optimal hyperparameters: direct estimation (McGuire & Segall, 2003) and maximum likelihood estimation (Segall & Matthews, 1997). Direct estimation is more compact and efficient but requires a denser and more stable observation network to get a reliable result. When combining the GPS and InSAR measurements, the direct estimation method is not very robust because the observation network is dramatically changing whenever an InSAR image is available, unless the time interval of an InSAR time series is comparable with GPS (e.g., weekly solution). Therefore, we choose the maximum likelihood estimation to estimate the optimal values of δ_m in our study.

3.4. Relative Weights Between Data Sets

Finally, when combining multiple data sets we apply a variance scaling on each data set, using the simplified Helmert Variance Component Estimation approach (Xu et al., 2009). From equation (2), we expect the data noise to be statistically described by the noise covariance matrix. In other words, the reduced chi-square of each data set properly weighted is expected to be equal to 1. The final scaling factor of each data set is computed using an iterative process, starting with equal scaling factors for all data sets. At each iteration, the scale factor of the data covariance matrix for each data set is the square root of the reduced chi-square, based on the residuals of the data type.

$$\sigma_j = \begin{cases} \sigma_j = 1, & j = 1 \\ \sqrt{\dfrac{\mathbf{v}_{j-1}^{\mathrm{T}}\mathbf{Q}\mathbf{v}_{j-1}}{n}}, & j > 1 \end{cases} \tag{3}$$

where j counts the iteration number; $\mathbf{v}$ is the residual for a given data type; n is the number of data; and $\mathbf{Q}$ is the inverse of the noise covariance matrix for that data. The residuals of the jth iteration, $\mathbf{v}_{j-1}$ were calculated with σ_{j-1} being the scale factor and then a new scale factor σ_j is calculated based on $\mathbf{v}_{j-1}$. The iteration stops when $\sigma_j = \sigma_{j-1}$.

4. Time-Dependent Source Models

In this section, we present the time-dependent source models that best fit the data in each case (i.e., GPS only, InSAR only, and GPS and InSAR jointly). We also describe how to determine the source geometry and the hyperparameters for each case. For the comparison with InSAR, we use the GPS data before 2016 because we do not have InSAR data after then.

4.1. GPS Only

For inverting the GPS data, we use the simplified spheroid model and estimate the axis ratio. Following the general source model for preeruptive deformation, we tried to invert a single Mogi source (the axis ratio is fixed to be 1). We found that a single Mogi source is not adequate to fit the data because of two main reasons. (1) With different initializations, either OKCE or OKNC will be underestimated. There are more than 10% of
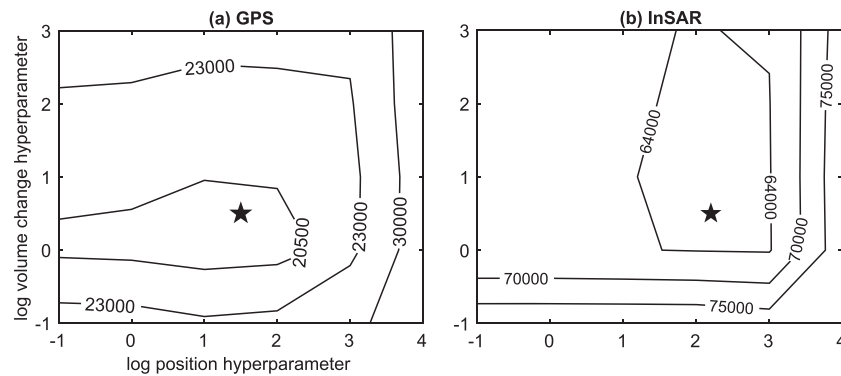
Figure 3. Likelihood (−2 L) contours as function of the hyperparameters for volume change and source location (a) when using GPS data only and (b) when using InSAR data only. Star markers represent the preferred model by maximum likelihood estimation.

the signals in the vertical component that are not captured, which is a large amount of signal considering the total magnitude of deformation at these two sites. (2) There were unreasonable shifts in the estimates of source location estimates when OKCE temporarily dropped out of the network in 2015, indicating that the OKCE and OKNC data are best fit by two different Mogi sources.

The next step is to determine the hyperparameters. We first estimate the axis ratio as a constant, which assumes the source shape does not change over time so that the corresponding hyperparameter is set to zero. Then, we assume the hyperparameters of the source location are same in the three components (east, north, and depth). Hence, there are two hyperparameters to be estimated—one for the source location and one for the volume change. We run a two-dimensional grid search and obtain the likelihood contour (Figure 3a). The preferred model is given at around (1e1.5, 1e0.5). Another take away from the likelihood contour is that a moving source may be not necessary because the likelihood stays almost the same even with a very small location hyperparameter (e.g., 0.1).

Figure 4 shows the estimates of the best fitting model. We can see only small variations less than 200 m in all the components of the source location. This is consistent with the maximum likelihood results that a relative stable source is indicated. On average, the source is estimated to be in the center of the caldera at ~2.6 km below the sea level. It is notable that the axis ratio is estimated to be ~0.5, which suggests an oblate spheroid source even taking into account the uncertainty. This geometry is quite different from a Mogi source and represents a substantial change in comparison to the preeruptive deformation pattern. The estimates of volume change match the temporal features in the time series at OKCE and OKNC. Similar to the preeruptive model, the GPS data indicate that the posteruptive model is spatially stable and the uplifts are mainly due to the volume increase.

4.2. InSAR Only

We invert only a Mogi source for the InSAR data. In other words, we fix the axis ratio to be 1. We first tried to model a simplified spheroid source as we did in the GPS-only inversion. The experiments showed that different initializations return similar estimates and overall goodness of fit, and the estimated axis ratio is always close to the initial value. This indicates that the InSAR data have poor constraints on the axis ratio because of lack of near-field observations (i.e., observations within the caldera region right above the volcanic sources).

The same method as for the GPS data is used to determine the optimal hyperparameters. According to the likelihood contour (Figure 3b), the preferred model is given at around (1e2.2, 1e0.5). Unlike with the GPS data, the InSAR data suggest a moving source because we do obtain a worse model with a very small hyperparameter for source location.

Figure 5 shows the estimates of the best fitting model. The model shows that the source moved to the south and to the east by about 1.5 km. This explains why the maximum likelihood solution favors a moving source. Similar horizontal motions were found for this data set by Qu et al. (2015) using a series of least squares inversions. In addition, the model shows a slow shallowing of the source.
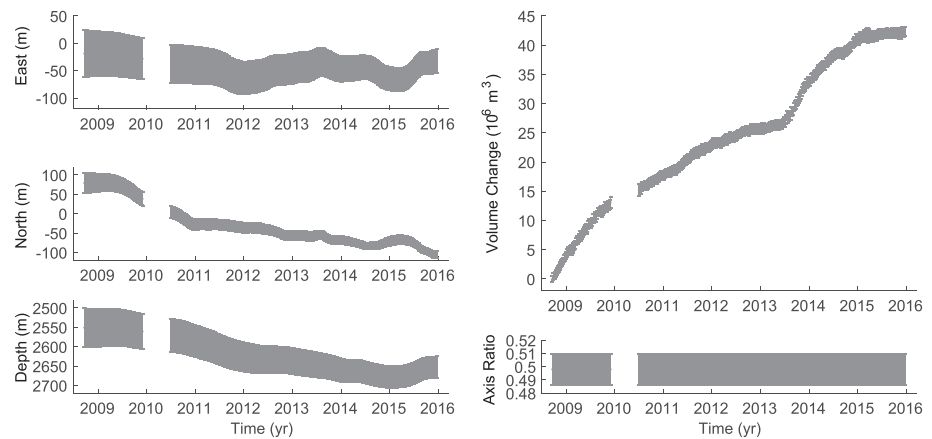
Figure 4. Time-dependent source model based on the GPS data only. All parameters are allowed to vary with time except for the ratio. The solid lines are the estimated values, and the error bars show 2σ uncertainties. The reference point of the Cartesian coordinate is the geometric center of the caldera. The volume change is assumed to be zero in the beginning.

4.3. GPS and InSAR

It is obvious that the best fit models for the GPS and InSAR data are not reconciled when inverting for a single volcanic source. Furthermore, we conduct some experiments showing that one spheroid source cannot fit the GPS and InSAR at the same time because there are always jumps in the estimates at the time of the InSAR data acquisitions. We can smooth down these jumps by using smaller hyperparameters, but the goodness of fit will be dramatically lower.

Recall the results of single inversions, the InSAR data suggest a Mogi source at 3–4 km depth. The source at such depth is consistent with the source determined for the preeruptive period, and it was commonly explained as a consistently replenished magma reservoir by previous studies (e.g., Lu & Dzurisin, 2014); the posteruptive source model should also consist of this structure. In Figure 5, we compare the InSAR model with the GPS model. It is noticeable that the InSAR model shows a deeper source than the GPS model but with slightly smaller volume changes. As a result, the InSAR model will most likely underpredict the GPS data, especially for OKCE. We therefore speculate that there should be shallower sources to account for additional and more localized deformation. Therefore, we propose a more complicated source geometry that consists of a Mogi source and a sill source.
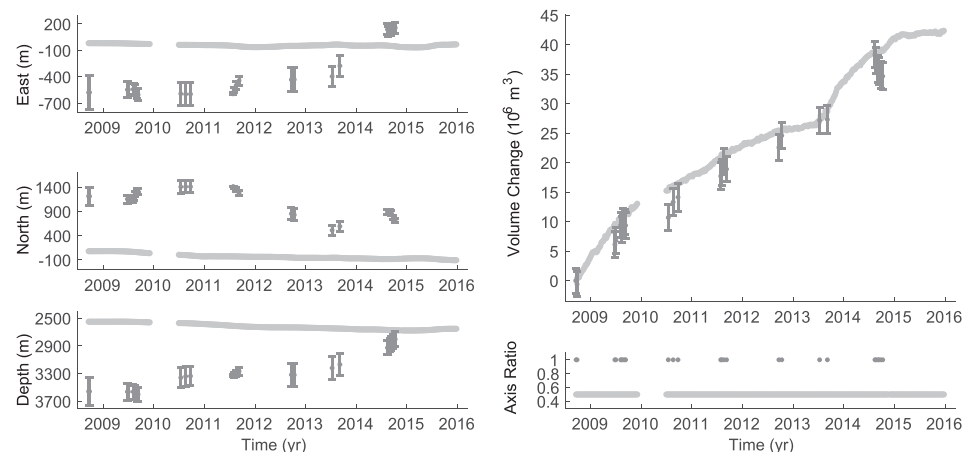

Figure 5. Time-dependent source model based on the InSAR data only. The axis ratio is fixed to be 1. The gray lines are the GPS estimates shown in Figure 4. The uncertainties of the GPS estimates are small and not shown here.
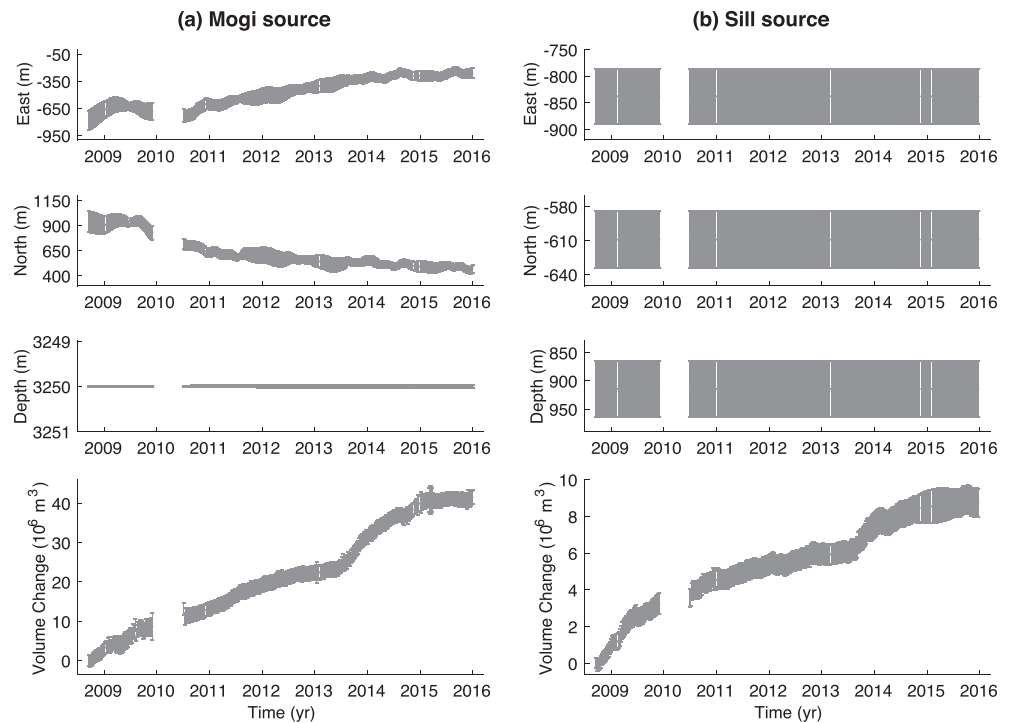
Figure 6. Time-dependent source model based on the GPS and InSAR data. (a) Estimates of the deep Mogi source. All the parameters are allowed to vary with time except for the depth. (b) Estimates of the shallow sill. All the parameters are estimated as constant except for the volume change.

We use a circular sill to represent a thin layer of magma here because this geometry has the fewest unknown parameters, but it could be a more complicated shape. Even though, it is still much more difficult to model two sources with the data because of the trade-offs between the source parameters. We take several measures to decrease the degrees of freedom in this scenario. First, we estimate the sill location to be constant rather than varying in time, which mitigates the trade-off between the Mogi source location and the sill location so that we can better separate the two sources. We think this is reasonable for two reasons: (1) we expect the shallow sill to be shallower than 2 km. At such a shallow depth, we think the sill should be a fairly stable structure in nature and separated from the Mogi source; (2) the GPS data should contain more information from this shallow sill, and only small variations in time are observed in the location estimates from GPS (Figure 4). Second, we run a series of inversions with the Mogi depth fixed ranging from 2.5 to 4.0 km. We find that the sill depth seems to be coupled with the Mogi source depth (Figure S7). The best model with minimum RMS value is obtained when the Mogi depth is fixed at ~3.2 km. In the final inversion, we thus fix the Mogi depth to be 3,250 m.

In terms of hyperparameters, we use same values for the sill as that for the spheroid source in the GPS-only inversion and the same values for the Mogi as that for the Mogi source in the InSAR-only inversion. Note that the location hyperparameter only applies to the horizontal location of the Mogi source since we fix the Mogi depth.

To assign the weights for each data set, we use the Helmert Variance Component Estimation method described in section 3.4. Because the time intervals of the GPS and InSAR measurements are so different (weekly vs yearly), here we rescale the data covariance based on the residuals of the complete filter run in time and apply a single scaling factor to each data set. The GPS scale factor is 1.12, indicating that the data noise covariance for GPS is closely true. The scale factors for the T93, T116, E115, and E222 covariance are 1.89, 1.45, 1.77, and 2.12, respectively.

Figure 6 shows the estimated parameters of the sill source and the Mogi source. The estimates of the Mogi source are similar to the InSAR model. The estimated sill is located to be centered at 53.422 N and
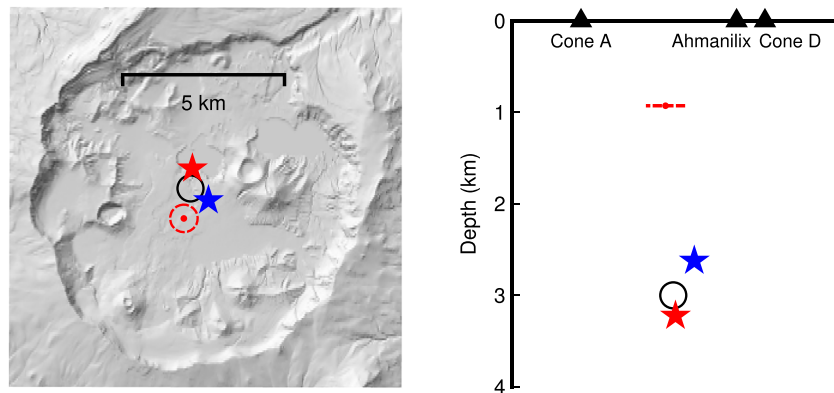
Figure 7. Geographic and depth map of the sources. The red star represents the Mogi source, and the red dashed circle (line) represents the sill source obtained by combining the GPS and InSAR data. The blue star is the spheroid source given by the GPS data. For comparison, the black circle denotes the preeruptive source. The Mogi source determined by the InSAR data only (section 4.2) is close to the Mogi source in the joint inversion (red star).

168.123 W, southwest of the geometric center of the caldera, and at ~0.9 km below sea level. The GPS residuals indicate an overall adequate fit of the source model (Figure 8a). Considering the InSAR residuals on the volcano flanks outside the caldera region, the model also provides a pretty good fit to the InSAR data (Figure 8b). We still calculate the InSAR residuals inside the caldera although we do not use these data. We can see that very large residuals stand out inside the caldera. We believe this is not overfitting but actual deformation associated with the new deposits ejected during the 2008 eruption. More discussions about it are in section 6.1.

This model fit both GPS and InSAR data very well and also explains why the GPS and InSAR data estimate two distinct sources: different coverages in space. The deformation caused by the shallow sill is mainly restricted to inside the caldera, while the deep Mogi source produces a long wavelength deformation pattern with comparable deformation inside and outside the caldera (Figure S6). The total deformation is the superposition of these two patterns. All the GPS sites are located inside the caldera or close to the caldera rim (Figure 1). It makes sense that the GPS-only inversion returns an oblate spheroid source whose location and shape is in between a sill and a Mogi source. The simulated experiments also support that the combination of a sill and a Mogi source will produce similar deformation at where the GPS sites are. In contrast, the majority of the InSAR coherent pixels lie on the volcano flanks and very few pixels are inside the caldera (Figure 2). Thus, the InSAR data do not contain much information from the shallow sill source. It is therefore not surprising that a single Mogi source is sufficient enough to fit the InSAR data.

5. Volume Change From 2008 to 2019

Another goal of this study is to track the volume change history since after the 2008 eruption. Having the source geometry determined, we then include the GPS data through 2019. From 2016 to 2019, the GPS data are from four continuous sites (OKNC, OKCE, OKSO, and OKFG). We fix the source location determined in section 4.3 (Figure 7) and estimate the total volume change from both sources.

Figure 10 shows the estimates of the total volume change. The kinematic volume changes reveal five consecutive exponential inflation episodes from 2008 to 2019. Each inflation episode begins with a rapid increase in volume and then slows down. We fit each of inflation episode using an exponential decay, that is, $\Delta V \cdot (1 - \exp(-t/\tau))$, where the characteristic timescale τ and characteristic strength ΔV are the two parameters estimated for each episode. From the first to the fifth inflation event, the characteristic timescale decreases from 1.5 to 0.3 year. From 2008–2019, the total volume change is about 0.068 km^3, of which 0.056 km^3 is from the deep Mogi source and 0.012 km^3 from the shallow sill. The volume change ratio between the deep Mogi source and the shallow sill source is about 5:1 through time.
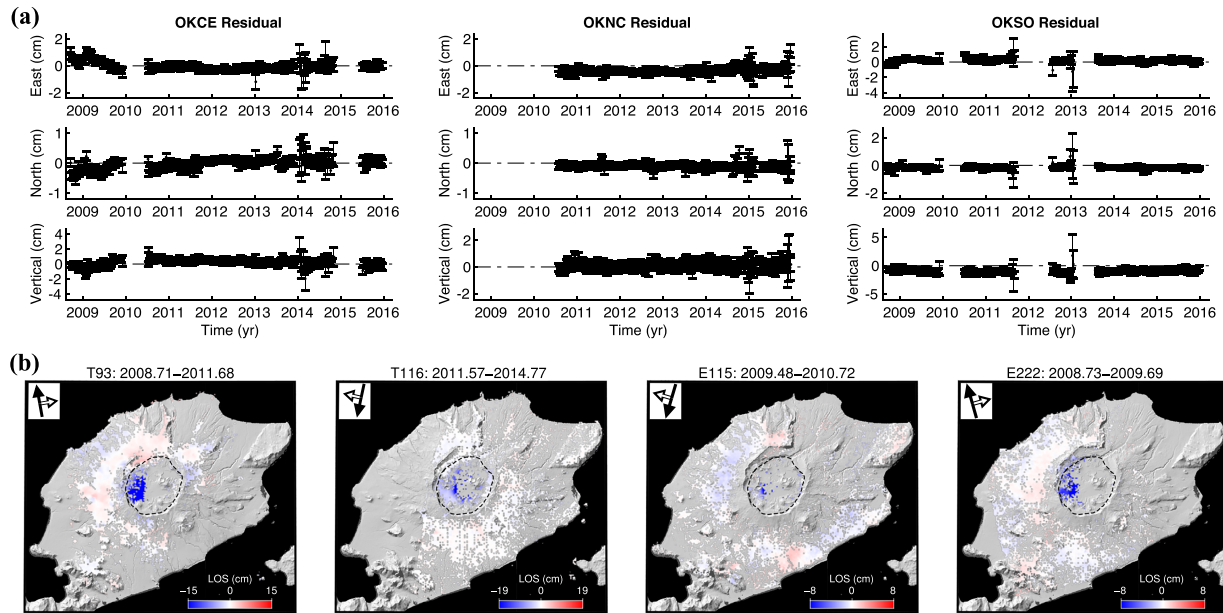
(a)

(b)

Figure 8. (a) Residuals of the GPS time series. (b) Residuals of selected interferograms in Figure 2. The linear phase ramp of each interferogram has been removed. The estimated initial position and the common mode have been removed for each GPS time series.

6. Discussion

6.1. Subsidence Within the Caldera Region

As shown in Figure 8b, the InSAR residuals within the caldera region are abnormally large. To compare InSAR with GPS, we project three-dimensional GPS measurements at OKNC and OKCE into the line-of-sight directions (Figure S5). The GPS data show obvious faster inflation than the surrounding InSAR measurements, especially at OKCE. We believe that the OKNC and OKCE measurements accurately record volcanic deformation as they are both installed on exposed solid rock. But most InSAR pixels inside the caldera are located on ground covered by the 2008 tephra deposits. It appears that these pixels measured not only the volcanic deformation but also significant localized deformation related to the 2008 tephra deposits and loose materials beneath that.

One of the possible causes is the self-compaction and erosion of new tephra deposits produced by the 2008 eruption. The caldera and eastern flank was blanketed by thick fine-grained tephra deposits. The thickest
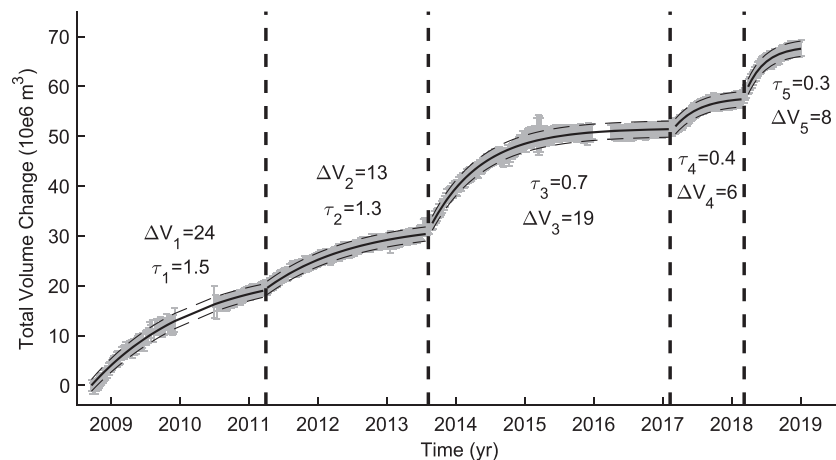

Figure 9. Total volume change from the sill and the Mogi source. The exponential fit and 95% confidence are denoted by solid and dashed lines, respectively. The timescale τ and characteristic strength ΔV of each inflation event is shown in the figure.
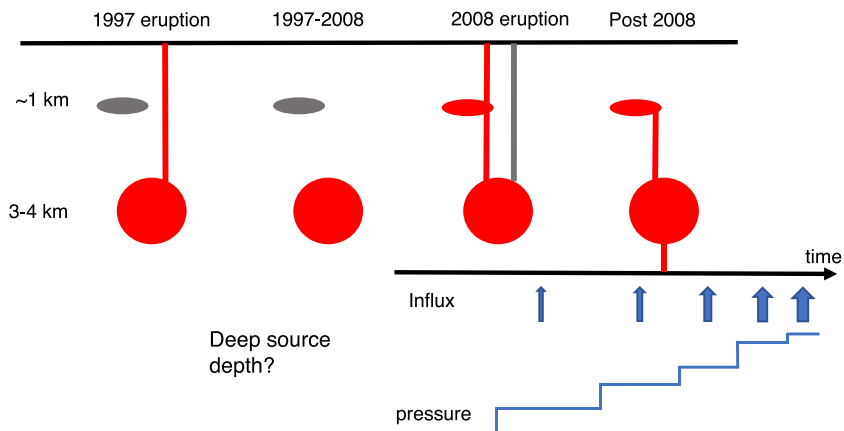
Figure 10. Conceptual model of the magma plumbing system at Okmok and dynamics of deep magma sources. The shallow sill source is inferred to have provided some magma (likely the more evolved component) for the 2008 eruption (Freymueller & Kaufman, 2010; Larsen et al., 2013) but had not been connected to the main shallow magma body prior to the 2008 eruption. Based on a hydraulic model (Lengliné et al., 2008), our results indicate that the pressure of the deep source may be episodic and the magma influx from the deep to shallow source may increase over time.

part is near the new cone exceeding 25–50 m thickness and thinning to centimeters thickness to the east (Larsen et al., 2015). The unconsolidated tephra deposits are subject to rapid compaction and are vulnerable to rapid remobilization by strong Aleutian rains and runoff from snow melt; significant erosion was observed in the field in the first few years after the eruption. From September 2008 to August 2010, the accumulation of sediments had enlarged the area of both intracaldera lakes (Larsen et al., 2015). Another possible cause is continued viscoelastic relaxation and thermo-elastic cooling from older flows that underlie the 2008 deposits. Localized subsidence inside the caldera was also observed between the 1997 and 2008 eruptions by Lu et al. (2005) in the region where the historical flows were emplaced. They explained the subsidence as the viscoelastic response of pre-1997 flows due to the loading of 1997 lava flow and the thermo-elastic contraction of 1958 lava flow. These two processes can cause subsidence of centimeters per year in the long term, and there is no reason that this deformation would have stopped after the 2008 eruption. We infer that the InSAR residuals also include the viscoelastic relaxation of the pre-2008 lava flows, especially the 1997 lava, due to loading of the newly emplaced 2008 tephra deposits and the thermo-elastic contraction of the 1997 lava flow.

In summary, we think that the large residuals within the caldera in InSAR data are likely sustained nonvolcanic deformation, such as self-compaction and viscoelastic relaxation. This is also the main reason why we masked out the InSAR pixels inside the caldera when doing the inversions.

6.2. Shallow Magma Sources

A long-lived spherical source at 3 km depth has been widely identified beneath Okmok volcano. It is likely that the Mogi source obtained in this study represents the same source that was found before the 2008 eruption, because of their close depths (Figure 8). The shallow sill obtained here is a new structure that was not seen in any preeruptive source models. To further prove that this is a substantial difference, we apply our method to the 1997–2008 data set and estimate a spheroidal source model instead of the Mogi source that is usually assumed in previous studies (Text S1). The best fit axis ratio is 1.1, which is very close to 1. This confirms the findings of the earlier studies that a single Mogi source explained the preeruptive deformation. By using a subset of the preeruptive data set and synthetic data, we also confirm that the change in the shallow system found in our study is not because of differences in the spatial sampling between the preeruptive and posteruptive data sets (Text S2).

Note that deflations of sill structures were inferred during the 2008 eruption. Using InSAR measurements, Lu and Dzurisin (2010) found closing of a rectangular sill at ~0.5 km depth during the 2008 eruption. They explained this structure as the extraction of groundwater related to the phreatic nature of the 2008 eruption. The shallow sill we obtained might be the same structure given the similarity in depths, but our results indicate that it is more likely a magma body or crystal mush that was drained in 2008 and has

been refilling after the 2008 eruption. Freymueller and Kaufman (2010) proposed that some of the 2008 magma had been resident at a shallower depth since before 1997, likely from an older preexisting magma body that was more chemically evolved (Larsen et al., 2013). The shallow sill source could represent the existing magma body these authors mentioned, which was drained during the 2008 eruption. During the 1997 eruption, Mann et al. (2002) also determined a collapsing sill at ~1.8 km depth along with a Mogi source for the coeruptive InSAR measurements.

We infer that Okmok's shallow plumbing system is composed of a stable magma chamber at about 3 km depth and some smaller magma storages at shallower depths. This is more in agreement with the petrological constraints (Larsen et al., 2013). Additionally, we infer that some of the shallow bodies are not fed during the intereruptive period, so are invisible from geodetic measurements, until they are somehow connected to other sources (e.g., due to eruptions). Our model supports that a shallow thin structure has become a part of the plumbing system and fed since the 2008 eruption. Another scenario is that the shallow magma bodies may not be sustained by the low pressure in the magma chamber after an eruption. For example, the sill found and determined by Mann et al. (2002) during the 1997 eruption might fully collapse as a single Mogi source was still able to well fit the data during the 1997–2008 period no matter what data type and spatial coverage.

6.3. Magma Supply Dynamics

An exponential inflation can be explained by a simple hydraulic model made up by a single shallow magmatic source fed by an infinite deep magma reservoir. If the deep magma reservoir is at a constant pressure, the shallow source will inflate exponentially until the pressure difference between the shallow source and deep reservoir vanishes (e.g., Pinel et al., 2010). Based on this hydraulic model, our kinematic volume change indicates that (1) the pressure of the deep source may increase episodically and (2) the influx from deep to shallow sources can increase with time at Okmok volcano.

First, the pressure of deep source must not be constant in time, which breaks the pressure balance between the shallow and deep sources. More specifically, we interpret that the pressure of the deep source increases in episodic pulses so that each new inflation episode occurs as a result of episodic magma supply into this deep source. Magma supply has been shown to be episodic not only at Okmok but also at other volcanoes. For example, before its 2010 eruption, repeated episodes of magma intrusion and accumulation were found beneath Eyjafjallajökull, Iceland (Sigmundsson et al., 2010). In the Aleutian arc, multiple episodic inflation events have been observed at Akutan volcano from 2005 to 2017 (DeGrandpre et al., 2017; Ji et al., 2017). Episodic inflation events are common at Kilauea volcano in Hawaii as well (e.g., Cervelli & Miklius, 2003); in that case, episodic deflation-inflation events were interpreted to result from short-lived blockages in the magma supply. Long-term episodic inflation pulses are also common at Kilauea and Mauna Loa (Poland et al., 2014).

Second, the influx from deep to shallow sources must not be constant in time. Otherwise, all the exponential inflating episodes should have the same timescale. As the exponential relaxation timescale (τ) is decreasing from earlier to later episodes, the influx should somehow increase in time. According to Lengliné et al. (2008), the influx or timescale is controlled by the radius of the shallow source (a_r) and width and depth of the conduit connected to the deep reservoir (a_c and H_c). Particularly, τ is proportional to a_r^3 and inversely proportional to a_c^4. This means that a small change of these two parameters may change the timescale in a significant way. In practice, we do not think a_r tends to be smaller in time. It is more likely that a_c increases in time, which would lead to more magma being able to flow through the conduit per unit time and thus a shorter timescale, but other parameter changes are possible. Alternative scenarios include the development and clearing of blockages in the magma transport system (Cervelli & Miklius, 2003) or the formation of additional conduits or dikes for each new pulse of magma from depth. Our present geodetic data are not sensitive to these parameters that limit our ability to test these alternate hypotheses.

6.4. How Close is Okmok to the Next Eruption?

In the current cycle, the volume withdrawal during the 2008 eruption is estimated to be 0.14 km^3 based on the InSAR measurements (Lu & Dzurisin, 2010) and 0.11 km^3 based on the GPS measurements (Freymueller & Kaufman, 2010) (the value was reported as 0.35 km^3 in the original paper, but the scaling between the Mogi source strength and volume change was accidentally applied twice; we reran the inversion using the

same data and correct the value here). By the beginning of 2019, we estimate that 0.068 km^3 of magma has been added since the 2008 eruption, which is 50–60% of the volume withdrawn during the eruption. Considering the previous eruptive cycle, the intereruptive volume increase from 1997 to 2008 was 85–100% of the 1997 eruption volume (Lu et al., 2010). This may imply that the capacity of Okmok magma storage system has a specific range, and an eruption will likely occur when the capacity is reached.

Additionally, the average inflation rate declined in time before the 1997 eruption and some oscillations (including episodes of deflation) were observed during 2004 to 2008 (Fournier et al., 2009; Lu et al., 2010). We have not yet seen deflationary features in the current cycle. It is unclear whether these features can be regarded as potential precursors. Future data should help uncover this question. However, kinematic models generally have a limited ability to forecast stability or instability of the magma system. More insights may be obtained by the use of physics-based models (e.g., Anderson & Segall, 2011), although those models have more degrees of freedom because of more unknown parameters and require caution in the basic understanding of the source geometry before using them.

7. Conclusion

In this paper, we introduce a time-dependent inversion filter combining InSAR with GPS for volcano deformation modeling. We model the posteruptive deformation at Okmok volcano, Alaska, based on the GPS and InSAR time series observations. We find that a Mogi source together with a shallow sill are required to explain both the GPS and InSAR data at the same time. The Mogi source determined here is close to the general preeruptive Mogi source that should represent the long-lived magma body that already existed since before the 1997 eruption. The shallow sill is likely an intrusion into a shallow space that was opened when an older, more evolved magma body was partially drained by the 2008 eruption. We infer that the shallow plumbing system of Okmok is more likely composed of multiple source at different depths. From the end of the 2008 eruption to 2019, the total volume increase is at least 50% of the 2008 volume decrease. We have identified five inflation episodes, each of which has the form of an exponential decay. The characteristic timescale of these inflation events is decreasing with time. We have not yet observed any oscillatory features such as those observed before the 2008 eruption. These features of the volume change curve may help us to understand more about eruptive cycle and unrest at Okmok volcano.

We demonstrate that combining GPS and InSAR is crucial to understand the shallow magma plumbing system of volcanoes. In the case of Okmok, the GPS data and the InSAR data individually suggest two distinct sources. We would not be able to figure out the "Mogi+sill" model without combining them. Besides, the InSAR time series techniques are getting more and more popular in volcano geodetic studies, and the time interval of InSAR acquisitions is becoming shorter and shorter with more InSAR sensors collecting data. There are high demands of an efficient workflow to take full advantage of time series observations from both GPS and InSAR. This paper presents a method for combining GPS and InSAR measurements to invert for the kinematics of volcanic source models. As the basis of the method is a type of Kalman filter, it also provides means of a near real-time tool for volcano hazards monitoring.

References

Albright, J. A., Gregg, P. M., Lu, Z., & Freymueller, J. T. (2019). Hindcasting magma reservoir stability preceding the 2008 eruption of Okmok, Alaska. *Geophysical Research Letters*, *46*(15), 8801–8808. https://doi.org/10.1029/2019GL083395

Anderson, K., & Segall, P. (2011). Physics-based models of ground deformation and extrusion rate at effusively erupting volcanoes. *Journal of Geophysical Research*, *116*, B07204. https://doi.org/10.1029/2010JB007939

Bartlow, N. M., Wallace, L. M., Beavan, R. J., Bannister, S., & Segall, P. (2014). Time-dependent modeling of slow slip events and associated seismicity and tremor at the Hikurangi subduction zone, New Zealand. *Journal of Geophysical Research: Solid Earth*, *119*, 734–753. https://doi.org/10.1002/2013JB010609

Bekaert, D. P. S., Segall, P., Wright, T. J., & Hooper, A. J. (2016). A network inversion filter combining GNSS and InSAR for tectonic slip modeling. *Journal of Geophysical Research - Solid Earth*, *121*(3), 2069–2086. https://doi.org/10.1002/2015JB012638

Biggs, J., Lu, Z., Fournier, T., & Freymueller, J. T. (2010). Magma flux at Okmok volcano, Alaska, from a joint inversion of continuous GPS, campaign GPS, and interferometric synthetic aperture radar. *Journal of Geophysical Research*, *115*, B12401. https://doi.org/10.1029/2010JB007577

Cervelli, P. (2013). Analytical expressions for deformation from an arbitrarily oriented spheroid in a half-space, EOS Transactions of the American Geophysical Union abstract V44C-06.

Cervelli, P., & Miklius, A. (2003). The shallow magmatic system of Kilauea Volcano. In C. Heliker, D. A. Swanson, & T. J. Takahashi (Eds.), *The Pu'u 'O'o-Kupaianaha eruption of Kilauea Volcano, Hawai'i: The first 20 years*, *U.S. Geological Survey Professional Paper, P1676* (pp. 149–163). Reston, VA: U.S. Geological Survey.

DeGrandpre, K., Wang, T., Lu, Z., & Freymueller, J. T. (2017). Episodic inflation and complex surface deformation of Akutan volcano, Alaska revealed from GPS time-series. *Journal of Volcanology and Geothermal Research*, *347*, 337–359. https://doi.org/10.1016/j.jvolgeores.2017.10.003

Fialko, Y., Khazan, Y., & Simons, M. (2001). Deformation due to a pressurized horizontal circular crack in an elastic half-space, with applications to volcano geodesy. *Geophysical Journal International*, *146*(1), 181–190. https://doi.org/10.1046/j.1365-246X.2001.00452.x

Fournier, T., Freymueller, J., & Cervelli, P. (2009). Tracking magma volume recovery at Okmok volcano using GPS and an unscented Kalman filter. *Journal of Geophysical Research*, *114*, B02405. https://doi.org/10.1029/2008JB005837

Freymueller, J. T., & Kaufman, A. M. (2010). Changes in the magma system during the 2008 eruption of Okmok volcano, Alaska, based on GPS measurements. *Journal of Geophysical Research*, *115*, B12415. https://doi.org/10.1029/2010JB007716

Fu, Y., & Freymueller, J. T. (2012). Seasonal and long-term vertical deformation in the Nepal Himalaya constrained by GPS and GRACE measurements. *Journal of Geophysical Research*, *117*, B03407. https://doi.org/10.1029/2011JB008925

Gregg, P. M., & Pettijohn, J. C. (2016). A multi-data stream assimilation framework for the assessment of volcanic unrest. *Journal of Volcanology and Geothermal Research*, *309*, 63–77. https://doi.org/10.1016/j.jvolgeores.2015.11.008

Ji, K. H., Yun, S.-H., & Rim, H. (2017). Episodic inflation events at Akutan Volcano, Alaska, during 2005–2017. *Geophysical Research Letters*, *44*(16), 8268–8275. https://doi.org/10.1002/2017GL074626

Julier, S. J., & Uhlmann, J. K. (2004). Unscented filtering and nonlinear estimation. *Proceedings of the IEEE*, *92*(3).

Larsen, J., Neal, C. A., Schaefer, J. R., Kaufman, A. M., & Lu, Z. (2015). *The 2008 phreatomagmatic eruption of Okmok Volcano*. Aleutian Islands, Alaska: Chronology, deposits, and landform changes.

Larsen, J., Śliwiński, M., Nye, C., Cameron, C., & Schaefer, J. (2013). The 2008 eruption of Okmok Volcano, Alaska: Petrological and geochemical constraints on the subsurface magma plumbing system. *Journal of Volcanology and Geothermal Research*, *264*, 85–106. https://doi.org/10.1016/j.jvolgeores.2013.07.003

Lengliné, O., Marsan, D., Got, J.-L., Pinel, V., Ferrazzini, V., & Okubo, P. G. (2008). Seismicity and deformation induced by magma accumulation at three basaltic volcanoes. *Journal of Geophysical Research*, *113*, B12305. https://doi.org/10.1029/2008JB005937

Lohman, R. B., & Simons, M. (2005). Some thoughts on the use of InSAR data to constrain models of surface deformation: Noise structure and data downsampling. *Geochemistry, Geophysics, Geosystems*, *6*, Q01007. https://doi.org/10.1029/2004GC000841

Lu, Z., & Dzurisin, D. (2010). Ground surface deformation patterns, magma supply, and magma storage at Okmok volcano, Alaska, from InSAR analysis: 2. Coeruptive deflation, July–August 2008. *Journal of Geophysical Research*, *115*, B00B02. https://doi.org/10.1029/2009JB006970

Lu, Z., & Dzurisin, D. (2014). *InSAR imaging of Aleutian volcanoes: monitoring a volcanic arc from space* (p. 419). Berlin, Heidelberg: Springer.

Lu, Z., Dzurisin, D., Biggs, J., Wicks, C., & McNutt, S. (2010). Ground surface deformation patterns, magma supply, and magma storage at Okmok volcano, Alaska, from InSAR analysis: 1. Intereruption deformation, 1997–2008. *Journal of Geophysical Research*, *115*, B00B02. https://doi.org/10.1029/2009JB006969

Lu, Z., Masterlark, T., & Dzurisin, D. (2005). Interferometric synthetic aperture radar study of Okmok volcano, Alaska, 1992–2003: Magma supply dynamics and postemplacement lava flow deformation. *Journal of Geophysical Research*, *110*, B02403. https://doi.org/10.1029/2004JB003148

Mann, D., Freymueller, J., & Lu, Z. (2002). Deformation associated with the 1997 eruption of Okmok volcano, Alaska. *Journal of Geophysical Research*, *107*(B4), 2072. https://doi.org/10.1029/2001JB000163

McGuire, J. J., & Segall, P. (2003). Imaging of aseismic fault slip transients recorded by dense geodetic networks. *Geophysical Journal International*, *155*(3), 778–788. https://doi.org/10.1111/j.1365-246X.2003.02022.x

Miller, T. P., McGimsey, R. G., Richter, D. H., Riehle, J. R., Nye, C. J., Yount, M. E., & Dumoulin, J. A. (1998). Catalog of the historically active volcanoes of Alaska, *Report Rep. 98-582*.

Mogi, K. (1958). Relations between the eruptions of various volcanoes and the deformations of the ground surfaces around them. *Bulletin of the Earthquake Research Institute*, *36*, 99–134.

Pinel, V., Jaupart, C., & Albino, F. (2010). On the relationship between cycles of eruptive activity and growth of a volcanic edifice. *Journal of Volcanology and Geothermal Research*, *194*(4), 150–164. https://doi.org/10.1016/j.jvolgeores.2010.05.006

Poland, M. P., Takahashi, T. J., & Landowski, C. M. (Eds) (2014). Characteristics of Hawaiian volcanoes, U.S. Geological Survey Professional Paper, 1801.

Qu, F., Lu, Z., Poland, M., Freymueller, J., Zhang, Q., & Jung, H.-S. (2015). Post-Eruptive Inflation of Okmok volcano, Alaska, from InSAR, 2008–2014. *Remote Sensing*, *7*(12), 15839.

Segall, P., & Matthews, M. (1997). Time dependent inversion of geodetic data. *Journal of Geophysical Research*, *102*(B10), 22,391–22,409. https://doi.org/10.1029/97JB01795

Sigmundsson, F., Hreinsdóttir, S., Hooper, A., Arnadóttir, T., Pedersen, R., Roberts, M. J., et al. (2010). Intrusion triggering of the 2010 Eyjafjallajökull explosive eruption. *Nature*, *468*(7322), 426–430. https://doi.org/10.1038/nature09558

Simons, M., Fialko, Y., & Rivera, L. (2002). Coseismic Deformation from the 1999 M_w 7.1 Hector Mine, California, earthquake as inferred from InSAR and GPS observations. *Bulletin of the Seismological Society of America*, *92*(4), 1390–1402. https://doi.org/10.1785/0120000933

Wan, E. A., & Van Der Merwe, R. (2000). The unscented Kalman filter for nonlinear estimation. *Proceedings of the IEEE*, *153-158*. https://doi.org/10.1109/asspcc.2000.882463

Xu, C., Ding, K., Cai, J., & Grafarend, E. W. (2009). Methods of determining weight scaling factors for geodetic–geophysical joint inversion. *Journal of Geodynamics*, *47*(1), 39–46. https://doi.org/10.1016/j.jog.2008.06.005

Yang, X.-M., Davis, P. M., & Dieterich, J. H. (1988). Deformation from inflation of a dipping finite prolate spheroid in an elastic half-space as a model for volcanic stressing. *Journal of Geophysical Research*, *93*(B5), 4249–4257. https://doi.org/10.1029/JB093iB05p04249

Zhan, Y., Gregg, P. M., Chaussard, E., & Aoki, Y. (2017). Sequential assimilation of volcanic monitoring data to quantify eruption potential: Application to Kerinci volcano, Sumatra. *Frontiers in Earth Science*, *5*(108). https://doi.org/10.3389/feart.2017.00108

Reference From the Supporting Information

Ohlendorf, S. J., Thurber, C. H., Pesicek, J. D., & Prejean, S. G. (2014). Seismicity and seismic structure at Okmok volcano, Alaska. *Journal of Volcanology and Geothermal Research*, *278-279*, 103–119. https://doi.org/10.1016/j.jvolgeores.2014.04.002